https://doi.org/10.1007/s41230-026-4218-2

Micro-alloying for improving corrosion resistance of as-cast alloy CoCrNi in 3.5wt.% NaCl solution by Ce addition

Bo Chen[1, 3], Chang Ma[1, 3], Wei-dong Xuan[2], Zhan-yong Gao[3], Guang-rui Zhang[4], **Fei Lu[5], and *Yuan Hou[1, 2, 3]

1. Analytical and Testing Center, Inner Mongolia University of Science and Technology, Baotou 014010, Inner Mongolia, China

2. State Key Laboratory of Advanced Special Steel, Shanghai University, Shanghai 200444, China

3. School of Materials and Metallurgy, Inner Mongolia University of Science and Technology, Baotou 014010, Inner Mongolia, China

4. Rare Earth Advanced Materials Technology Innovation Center, Baotou 014030, Inner Mongolia, China

5. State Key Laboratory of Baiyunobo Rare Earth Resource Researches and Comprehensive Utilization, Baotou Research Institute of Rare Earths, Baotou 014030, Inner Mongolia, China

Abstract: Enhancing corrosion resistance in cast alloys using straightforward and cost-effective micro-alloying techniques has emerged as a key area of investigation in materials science. The challenge lies in applying this technique to further enhance the already excellent properties of CoCrNi medium-entropy alloys (MEAs) for casting applications. A micro-alloying approach was proposed to improve the corrosion resistance of as-cast CoCrNi MEAs by incorporating cerium (Ce). The corrosion resistance of CoCrNi MEAs firstly increases and then decreases as the Ce content increases in a 3.5wt.% NaCl solution. At a Ce content of 0.02at.%, the passivation current density reaches its minimum value (26.383 μA·cm^{-2}), while the breakdown potential reaches its maximum (0.471 V_{SCE}), imparting exceptional corrosion resistance. The results indicate that the enhanced corrosion resistance is primary due to Ce micro-alloying, which affects inclusions by forming a non-conductive precipitated phase and modifying the passivation film. Ce micro-alloying presents a promising strategy for enhancing the corrosion resistance of as-cast CoCrNi MEAs.

Keywords: medium-entropy alloys; as-cast; rare earth micro-alloying; corrosion resistance

CLC numbers: TG146.1$^+$6 **Document code:** A **Article ID:** 1672-6421(2026)02-233-12

1 Introduction

Medium entropy alloys (MEAs), especially those based on CoCrNi, have gained significant attention in materials science due to their unique combination of properties[1-6]. CoCrNi MEAs, characterized by a nearly equiatomic composition of cobalt (Co), chromium (Cr), and nickel (Ni), offer an advantageous balance of mechanical strength, ductility, and resistance to high-temperature oxidation and corrosion, setting them apart from conventional alloys[7-13]. Moreover, corrosion resistance plays a critical role in determining the durability and reliability of cast alloys in various industrial settings, including aerospace, automotive, and marine environments[14]. Enhanced corrosion resistance can extend service life, reduce maintenance costs, and elevate safety standards, making it a focal point of ongoing research. Consequently, the development of innovative alloying strategies remains essential to further improve the corrosion resistance of these advanced materials.

Micro-alloying, which involves the addition of trace amounts of specific elements (<0.1%), introduces an innovative strategy for enhancing the properties of alloys. This technique can profoundly affect the microstructure and phase constitution of the base alloy, ultimately leading to superior performance attributes. Whether incorporating rare-earth elements (REs) or common metallic elements, such as aluminum (Al),

*Yuan Hou

Ph. D., Associate Researcher. His research interests mainly focus on the study of the mechanism of magnetic field and rare-earth microalloying to modulate the phase transformation of metals.

E-mail: houyuan@imust.edu.cn

**Fei Lu

E-mail: yurifeiphy@126.com

Received: 2024-10-12; Revised: 2024-11-15; Accepted: 2024-11-25

iron (Fe), Cr, or Ni, the objective is to optimally dope MEAs and high-entropy alloys (HEAs)[15-19]. Presently, additional research is imperative to comprehensively understand the utilization of REs, specifically cerium (Ce)-doped MEAs/HEAs. Improving the corrosion resistance of MEAs/HEAs is a paramount objective, and the potential for enhancing other properties through the incorporation of REs merits further exploration. Furthermore, if the addition of REs proves equally effective in bolstering other properties, their cost implications must also be taken into account. The incorporation of REs is recognized for refining grain structures, augmenting mechanical properties, and substantially enhancing corrosion resistance. Notably, Ce has demonstrated remarkable effects on the corrosion resistance of metallic alloys[20-23]. It is well-documented that Ce promotes the formation of fine, equiaxed grains during solidification, which can enhance the mechanical properties and uniformity of the alloy. Moreover, Ce can form stable oxides that serve as protective barriers on the alloy surface, thereby augmenting its resistance to corrosion. For instance, Ce has been successfully employed to enhance the corrosion resistance of aluminum, magnesium, and steel alloys by forming a stable and adherent oxide layer that safeguards the underlying metal from corrosive environments[24, 25].

Research on the specific impacts of Ce on CoCrNi MEAs is still in its nascent stages. Preliminary studies have indicated substantial potential for enhancing mechanical strength, ductility, and resistance to high-temperature oxidation. The present research endeavors to investigate the influence of Ce micro-alloying on the corrosion resistance of CoCrNi MEAs and to elucidate the mechanisms by which the addition of Ce improves the alloy's performance. The insights garnered from this research can pave the way for the development of more resilient and corrosion-resistant cast alloys through micro-alloying, thereby broadening the application scope of medium entropy alloys in harsh environments.

2 Experimental processes

2.1 Material preparation

CoCrNi MEAs with varying Ce concentrations were prepared through vacuum induction melting in an argon atmosphere. High-purity metals, specifically Co, Cr, Ni, and Ce (all with a purity>99.9%), were selected as raw materials. To ensure homogeneity, each Ce micro-alloyed MEA underwent multiple melting and re-melting cycles, typically four to five times. The molten alloys (melting temperature of about 1,500 °C) were then poured into water-cooled copper molds at about 1,450 °C using suction casting, producing alloy ingots with dimensions of 10 mm×10 mm×50 mm. Table 1 presents the nominal and actual chemical compositions of the Ce micro-alloyed MEAs (designated Ce-0, Ce-1, and Ce-2), where actual chemical compositions were determined by inductively coupled plasma-atomic emission spectrometry (ICP-ATES, Agilent 5110). The ingots were solution treated at 1,200 °C for 24 h, followed by water quenching.

Table 1: Nominal and actual chemical compositions of CoCrNi MEAs with varying Ce contents (at.%)

Alloys		Co	Cr	Ni	Ce
Ce-0	Nominal	33.33	33.33	33.33	
	Actual	34.13	33.34	32.54	
Ce-1	Nominal	33.31	33.31	33.31	0.07
	Actual	33.41	33.02	33.55	0.02
Ce-2	Nominal	33.20	33.20	33.20	0.40
	Actual	33.32	32.92	33.42	0.34

2.2 Characterization

2.2.1 Electrochemical tests

Test specimens (10 mm×10 mm×3 mm) for electrochemical analysis were sectioned from suction-cast samples using electrical discharge machining wire cutting. The specimens were polished sequentially with SiC papers of increasing grit (#400 to #2000), followed by polishing with a 2.5 μm diamond suspension, and then thoroughly cleaned and dried using deionized water and anhydrous ethanol by a conventional hair dryer.

Electrochemical tests were conducted in a 3.5wt.% NaCl solution using a CHI760E electrochemical workstation. A three-electrode setup was employed, comprising the Ce micro-alloyed MEA sample as the working electrode (electrochemical surface area about 0.196 cm^2), a platinum wire as the counter electrode, and a saturated calomel electrode (SCE) as the reference electrode. Before testing, samples were immersed in the 3.5wt.% NaCl solution for 2 h to stabilize the open circuit potential (OCP). Potentiodynamic polarization curves were then recorded by scanning the potential from −1.0 V_{SCE} to 1.0 V_{SCE} at 1 $mV \cdot s^{-1}$. Additionally, electrochemical impedance spectroscopy (EIS) was conducted over a frequency range of 10^5 Hz to 10^{-2} Hz using a 5 mV sinusoidal perturbation. Data were fitted using a ZSimpWin software. All tests were performed at room temperature.

2.2.2 Microstructure characterization

The crystal structures and phase constitutions of the alloys were analyzed via X-ray diffraction (XRD) using a Japan Rigaku Smartlab diffractometer (Cu Kα radiation) at a scanning rate of $10° \cdot min^{-1}$ across a 2θ range of 20° to 90°. The alloy microstructures were examined using field emission scanning electron microscopy (FE-SEM, GAIA3 XMN) and energy-dispersive X-ray spectroscopy (EDS) to observe grain structure, while the distribution of Ce was analyzed using an electron probe X-ray microanalyzer (EPMA, JXA-iHP200F). Detailed microstructural observations were further conducted using a transmission electron microscope (TEM, Talos F200X).

2.2.3 Passive film analysis

X-ray photoelectron spectroscopy (XPS, ESCALAB Xi+) was

utilized to investigate the chemical properties of the oxide layers on the surface of the alloys, focusing on passive film composition. Testing samples were immersed in the 3.5wt.% NaCl solution for 7 days to promote the formation of a stable passivation film on the surface of the Ce micro-alloyed MEAs. XPS data were processed using Thermo Avantage software (Version 5.52), with binding energies calibrated against the C 1s peak at 284.8 eV.

3 Results and discussion

3.1 Microstructural characterization

The crystal structures and phase constitutions of as-cast CoCrNi MEAs with varying Ce contents were examined by XRD, as shown in Fig. 1. The diffraction peaks observed across all Ce-doped MEAs align with the characteristic of face-centered cubic (FCC) phase, indicating that these alloys retain a typical FCC solid solution structure. With increasing Ce content, the diffraction peak intensities show notable variations. Specifically, the intensities of the (111) and (311) peaks augment, whereas those of (200) and (220) peaks diminish. Notably, no peak shifts are observed. The atomic radius of Ce is significantly different from that of Co, Cr, and Ni, the atomic radius of Ce is larger than that of Co, Cr, and Ni. When Ce is added to CoCrNi MEAs, it induces lattice distortion due to the size mismatch. This lattice distortion alters the local atomic arrangement, leading to changes in the lattice constant, which in turn influences the intensity of the XRD diffraction peaks.

Figure 2 displays SEM images of CoCrNi MEAs with different Ce concentrations. The images reveal the presence of second-phase precipitates in all CoCrNi MEAs, exhibiting

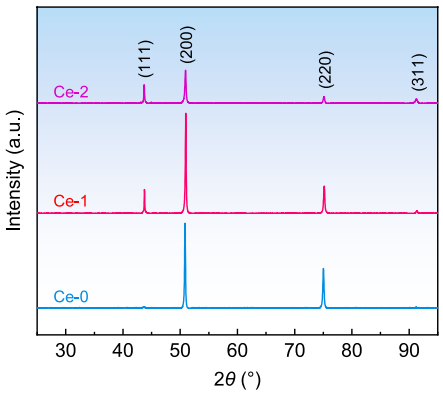

Fig. 1: XRD patterns of CoCrNi MEAs with varying Ce contents

variations in morphology and size. Specifically, precipitates in Ce-0 exhibit irregular, elongated morphologies; those in Ce-1 are spherical; and in Ce-2 are dendritic structures. Additionally, the precipitate distribution in the Ce-1 and Ce-2 alloys shows an uneven dispersion across the alloy matrix. At a lower Ce concentration (0.02at.%), precipitates are randomly distributed, while at a higher concentration (0.34at.%), they preferentially form along interdendritic regions.

EDS analysis of the alloy matrix and precipitates conducted in Fig. 2 (refer to Table 2) reveals that the precipitates in the Ce-0 alloy are primarily composed of Hf, Zr, and O, suggesting contamination from raw material impurities. In contrast, the precipitates in the Ce-1 and Ce-2 alloys are Ce-containing second phases, with no detectable Ce in the alloy matrix. This indicates that Ce predominantly exists in the precipitated form within Ce micro-alloyed MEAs. Furthermore, as the Ce concentration increases, both the Ce content and the number of precipitates increase significantly, consistent with previous research on rare-earth element-doped CoCrNi MEAs[26, 27].

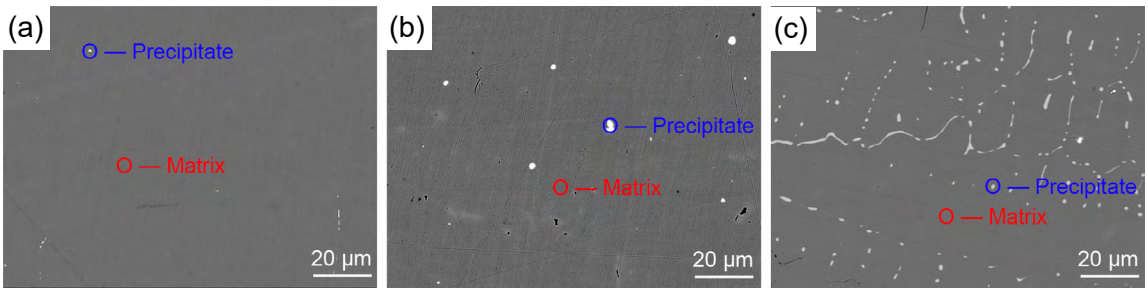

Fig. 2: SEM images of CoCrNi MEAs with varying Ce contents: (a) Ce-0; (b) Ce-1; (c) Ce-2

Table 2: EDS results of CoCrNi MEAs with different Ce contents in Fig. 2

Alloys	Regions	Elements (at.%)						
		Co	Cr	Ni	Ce	O	Hf	Zr
Ce-0	Matrix	24.55	42.28	33.17				
	Precipitates	2.67	2.56	0.52		10.77	65.74	17.75
Ce-1	Matrix	24.29	38.36	37.36				
	Precipitates	17.07	42.06	30.51	10.36			
Ce-2	Matrix	24.05	39.12	36.83				
	Precipitates	7.00	2.01	58.17	32.82			

To further elucidate the elemental distribution within Ce micro-alloyed MEAs, EPMA was performed, with the results presented in Fig. 3. The elemental maps reveal that, in all the alloys, Co, Cr, and Ni are uniformly distributed across the matrix, with no significant segregation observed, indicating that these elements maintain a solid solution in the matrix. In the Ce-0 alloy, the distribution of Hf and Zr is closely associated with the white precipitates, which correspond to oxide inclusions. In contrast, in the Ce-1 and Ce-2 alloys, the properties of the white precipitates changes significantly. Due to the high reactivity of Ce with oxygen, the addition of Ce results in the formation of stable Ce oxides, and these Ce-rich oxides are thermodynamically favorable. High chemical activity of Ce leads to its rapid oxidation upon cooling, forming CeO_2 or other Ce oxide phases. Unlike Hf and Zr, which are relatively inert in the formation of oxide inclusions, Ce readily forms stable oxide particles that precipitate within the matrix. This change in precipitate composition is a direct result of the addition of Ce, which alters the properties of the inclusions and modifies the phase distribution within the alloy[28-30].

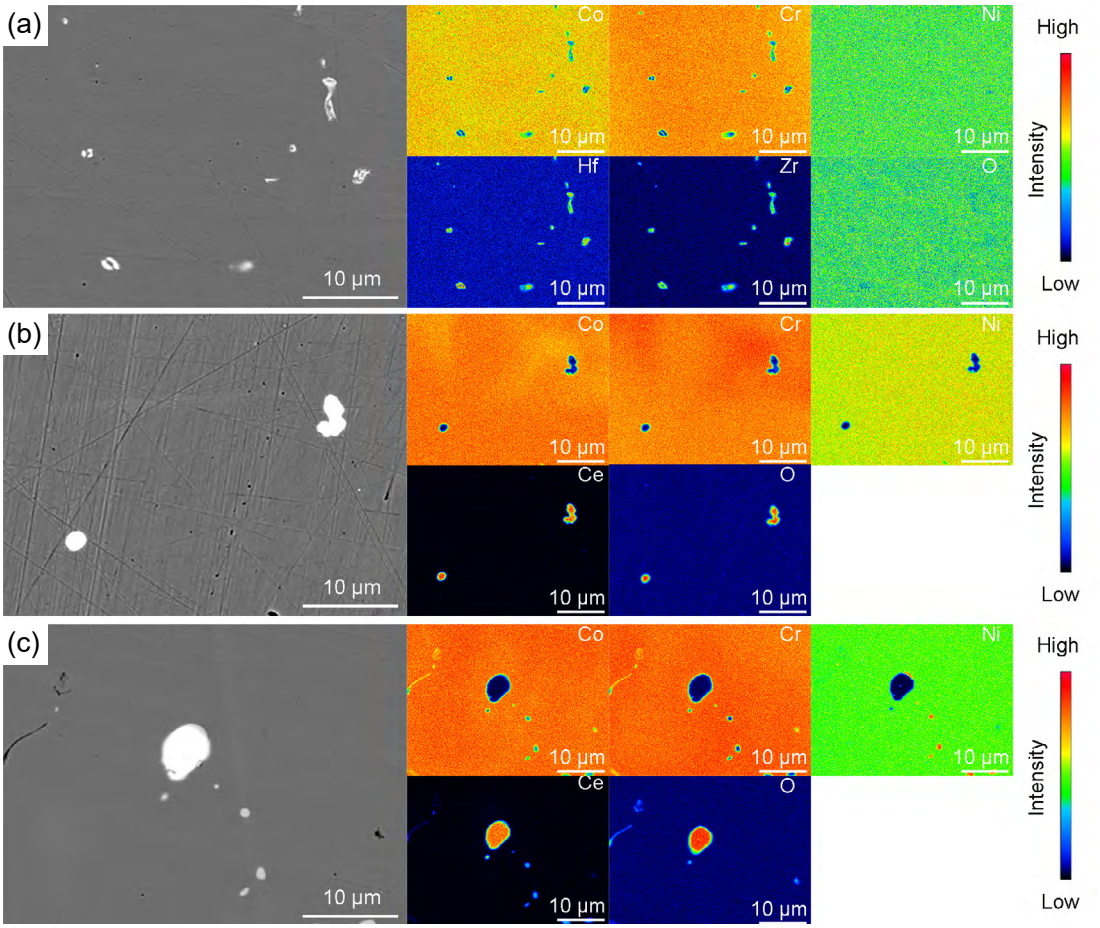

Fig. 3: Elemental distribution plots of CoCrNi MEAs with different Ce contents: (a) Ce-0; (b) Ce-1; (c) Ce-2

TEM analysis of the precipitates in the Ce-1 alloy (Fig. 4) reveals a distinct core-shell structure, characterized by a central Ce-O oxide core surrounded by a Ce-O-S compound shell. The core-shell structure is clearly depicted in the high-magnification bright-field (BF) TEM image, with corresponding EDS elemental mapping revealing a distinct spatial distribution of O and S [Fig. 4(a)]. Specifically, the EDS maps show a concentrated region of O in the core area, surrounded by an enriched region of both O and S in the shell. This observation suggests a sequential precipitation process, where the Ce-O phase forms firstly, and a secondary phase rich in Ce-O-S gradually deposits around it.

The high-angle annular dark-field (HAADF) imaging shown in Fig. 4(b) provides additional contrast that highlights the differences in atomic number across the core and shell regions, further emphasizing the distinct phases within the precipitate. Further investigation into the core-shell structure of the precipitates was performed using high-resolution transmission electron microscopy (HRTEM) and associated selected area electron diffraction (SAED). HRTEM images, as illustrated in Figs. 4(c) and (d), clearly show lattice fringes corresponding to well-defined crystallographic planes, providing a deeper insight into the crystalline nature of the precipitated phases. The diffraction patterns taken from both the core and shell regions exhibit characteristic spots consistent with a FCC structure. The FCC diffraction patterns obtained from the precipitates indicate that, despite the compositional differences between the matrix and precipitates, there is crystallographic coherence between these phases. The SAED patterns from the precipitates match those of an FCC lattice, consistent with the XRD results presented in Fig. 1.

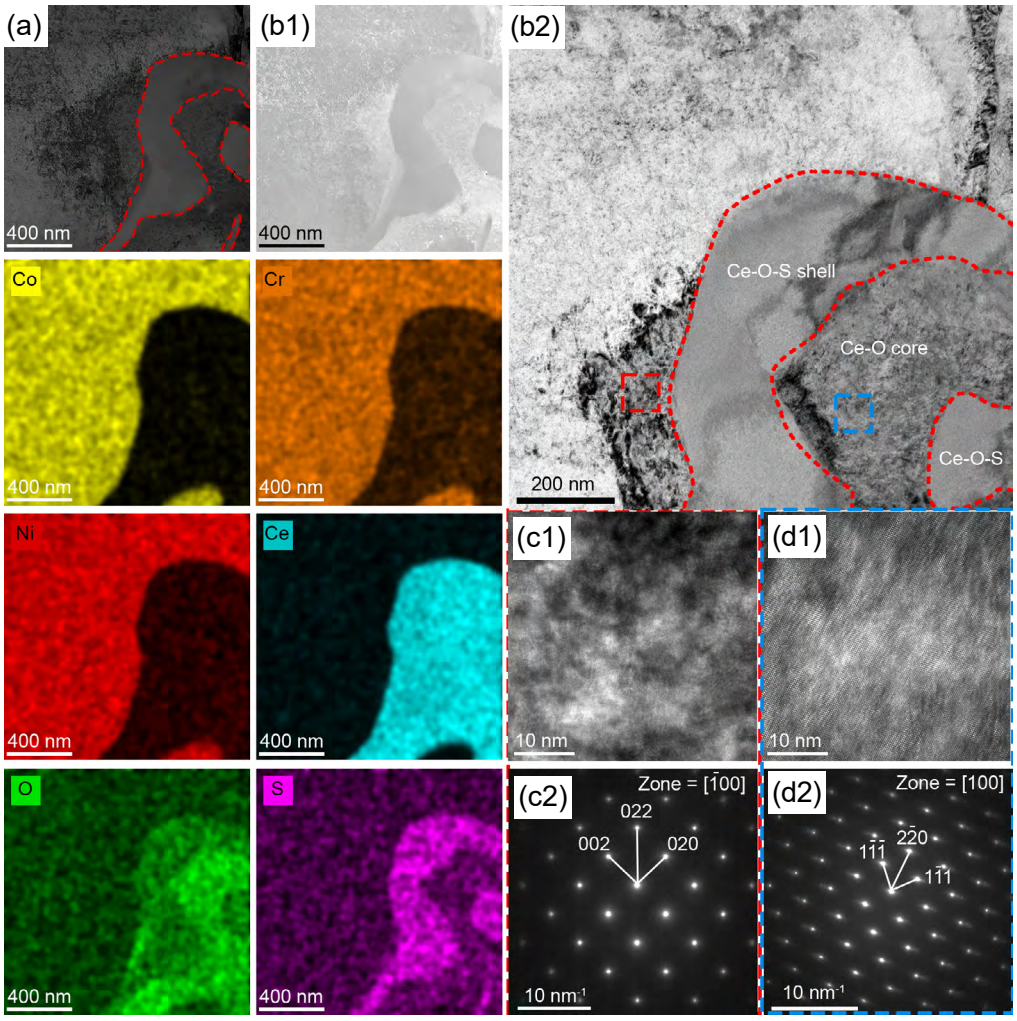

Fig. 4: TEM results of precipitated phases in Ce-1 alloy: (a) high magnification BF image and TEM-EDS mappings; (b) HAADF image; (c) and (d) HRTEM images and associated diffraction patterns of matrix and precipitation

This unique structural formation arises from the strong affinity of REs for both O and S. Given the high chemical reactivity of Ce with these elements, a stable Ce-O oxide core forms initially, followed by the subsequent precipitation of a Ce-O-S shell during the solidification process. This layer-by-layer segregation process is driven by thermodynamic stability considerations, where Ce forms highly stable oxides, and S, which exhibits a weaker affinity compared to O, becomes enriched at the oxide boundary. Consequently, the formation of this core-shell precipitate architecture is influenced by the kinetic conditions during cooling and the inherent affinity of REs to form stable compounds, in line with previously reported findings[23, 31].

3.2 Corrosion behavior

Figure 5 depicts the corrosion behavior of CoCrNi MEAs with varying Ce contents in a 3.5wt.% NaCl solution. The potentiodynamic polarization curves presented in Fig. 5(a) reveal that all the three Ce micro-alloyed MEAs, regardless of their Ce concentrations, exhibit similar polarization characteristics and possess a distinct passivation region. The results of the fitted electrochemical parameters are summarized in Table 3, which includes the self-corrosion potential (E_{corr}), self-corrosion current density (I_{corr}), primary passivation potential (E_{pp}), passivation current density (I_{pass}), breakdown potential (E_b), and passivation range ($\Delta E=E_b-E_{pp}$). Notably, the Ce-1 alloy boasts the broadest passivation range of 0.996 V_{SCE}, suggesting its superior capacity to form a stable passivation film. In contrast, the Ce-2 alloy exhibits a narrower passivation range of 0.399 V_{SCE}, accompanied by a sharp increase in current density, indicative of passivation film damage and subsequent failure, leading to decreased corrosion resistance[7, 32].

As the Ce content increases, the E_{corr} value of Ce micro-alloyed MEAs gradually rises, while the I_{corr} value exhibits an initial increase followed by a decrease. Generally, a higher E_{corr} value suggests a reduced thermodynamic tendency for corrosion, whereas a lower I_{corr} value signifies a slower corrosion rate[33, 34]. However, the presence of a passivation film on Ce micro-alloyed MEAs necessitates the consideration of additional parameters beyond E_{corr} and I_{corr} for illustrating the alloy's corrosion performance. I_{pass} and E_b are crucial parameters for assessing the corrosion resistance of alloys with passivation films, as they are intimately linked to the

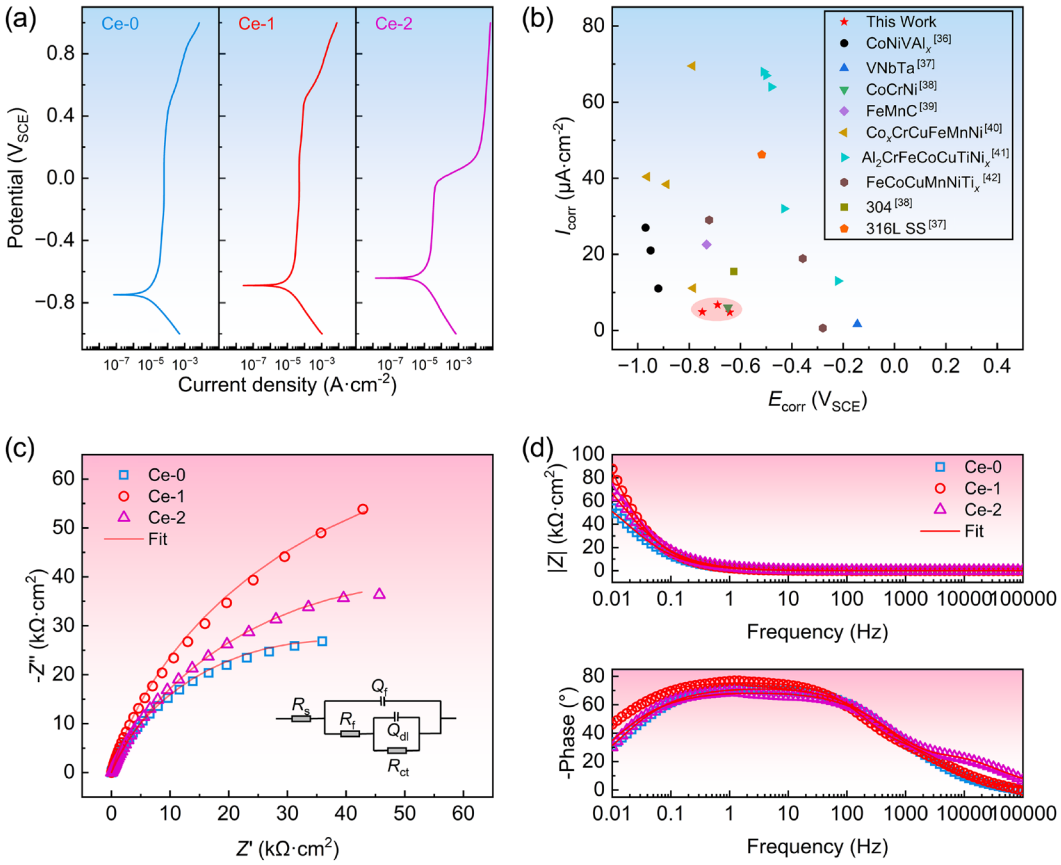

Fig. 5: Corrosion behavior of CoCrNi MEAs with different Ce contents in 3.5wt.% NaCl solution: (a) Tafel plots; (b) comparison of E_{corr}, I_{corr} of different alloys in 3.5wt.% NaCl solution; (c) Nyquist plots; (d) Bode plots

stability of the film[35]. The magnitude of I_{pass} approximately indicates the dissolution rate of the passivation film, whereas the magnitude of E_b signifies the stability of the film. According to Table 3, the I_{pass} values follow an ascending order of Ce-1<Ce-2<Ce-0, while the E_b values exhibit a descending order of Ce-1>Ce-0>Ce-2. Despite the Ce-2 alloy exhibiting the lowest E_b, it demonstrates a higher E_{corr} and lower I_{corr} and I_{pass} compared to the Ce-0 alloy. Thus, in a comprehensive comparison based on multiple parameters including E_{corr}, I_{corr}, I_{pass}, and E_b, the corrosion resistance of the Ce micro-alloyed MEAs follows the order: Ce-1>Ce-2>Ce-0. The superior corrosion performance of the Ce-1 alloy underscores the effectiveness of micro-alloying with ≤0.02at.% Ce in enhancing corrosion resistance, whereas further addition of Ce results in a notable decrease in corrosion resistance.

To emphasize the superior corrosion resistance of the studied Ce micro-alloyed MEAs system, Fig. 5(b) presents a comparison of its I_{corr} and E_{corr} in a 3.5wt.% NaCl solution with other MEAs, HEAs, and stainless steels (304 and 316 SS)[36-42]. According to the data, the Ce micro-alloyed MEAs in this study exhibit a corrosion current density of approximately 6 μA·cm^{-2}, which is notably lower than the 11 μA·cm^{-2} observed in other MEAs and the 11 μA·cm^{-2} in HEAs. Even when compared to commonly used stainless steels like 304 SS (with a corrosion current density of around 15 μA·cm^{-2}) and 316 SS (about 46 μA·cm^{-2}), the Ce micro-alloyed MEAs show a lower corrosion current density. These detailed comparisons are also provided in Table 4. Clearly, the incorporation of Ce as a micro-alloying element offers a potent approach to enhancing the corrosion resistance of as-cast CoCrNi MEAs.

Table 3: Electrochemical parameters obtained from polarization curve of Ce-0, Ce-1, and Ce-2

Alloys	E_{corr} (V$_{SCE}$)	I_{corr} (μA·cm^{-2})	E_{pp} (V$_{SCE}$)	I_{pass} (μA·cm^{-2})	E_b (V$_{SCE}$)	ΔE (V$_{SCE}$)
Ce-0	−0.749	4.833	−0.529	34.475	0.436	0.965
Ce-1	−0.689	6.698	−0.525	26.383	0.471	0.996
Ce-2	−0.642	4.758	−0.474	34.314	−0.075	0.399

The EIS results depicted in Figs. 5(c, d) reveal a consistent pattern among all the Ce micro-alloyed MEAs, regardless of their Ce content. Specifically, all the alloys display Nyquist plots characterized by semi-circular capacitive arcs, which suggest a uniform corrosion mechanism across the different samples. However, there are noticeable differences in the radii of these capacitive arcs. As the Ce content increases, the radii of the arcs firstly expand and then diminish. Generally, a larger arc radius is indicative of higher resistance to corrosion, which translates to better material corrosion resistance[43, 44]. Based on this observation, the Ce-1 alloy stands out as it exhibits the largest arc radius, indicating that it possesses superior corrosion resistance compared to the other alloys in this study.

Table 4: E_{corr} and I_{corr} of different MEAs, HEAs, and stainless steels (304 and 316 SS) in a 3.5wt.% NaCl solution

Alloys	E_{corr} (V)	I_{corr} (μA·cm^{-2})	References
CoNiV	−0.970	27.000	Ref. 36
$(CoNiV)_{97}Al_3$	−0.950	21.000	
$(CoNiV)_{95}Al_5$	−0.920	11.000	
VNbTa	−0.145	1.637	Ref. 37
316 SS	−0.517	46.190	
CoCrNi	−0.649	6.013	Ref. 38
304	−0.626	15.500	
FeMnC	−0.732	22.560	Ref. 39
$Co_{0.5}CrCuFeMnNi$	−0.964	40.400	Ref. 40
$Co_{1.0}CrCuFeMnNi$	−0.888	38.400	
$Co_{1.5}CrCuFeMnNi$	−0.785	11.100	
$Co_{2.0}CrCuFeMnNi$	−0.787	68.500	
$Al_2CrFeCoCuTiNi$	−0.510	68.000	Ref. 41
$Al_2CrFeCoCuTiNi_{0.5}$	−0.430	32.000	
$Al_2CrFeCoCuTiNi_{1.0}$	−0.220	13.000	
$Al_2CrFeCoCuTiNi_{1.5}$	−0.480	64.000	
$Al_2CrFeCoCuTiNi_{2.0}$	−0.500	67.000	
FeCoCuMnNiTi	−0.279	0.630	Ref. 42
$FeCoCuMnNiTi_{0.1}$	−0.357	18.900	
$FeCoCuMnNiTi_{0.2}$	−0.722	29.000	

The Bode plot in Fig. 5(d) displays the impedance modulus ($|Z|$) versus frequency, along with the phase angle. It is noteworthy that the value of $|Z|$ at the lowest frequency (f=0.01 Hz) approximates the charge transfer resistance. A larger impedance value signifies a higher charge transfer resistance and, consequently, better corrosion resistance of the alloy[45]. Furthermore, the phase angle Bode plots of all alloys exhibit distinct peaks in the mid-frequency region. Specifically, the Ce-1 alloy demonstrates a maximum phase angle of not less than 75°, whereas the Ce-0 and Ce-2 alloys exhibit phase angles not exceeding 70°. Larger phase angles are indicative of superior corrosion resistance of the passivation film[45]. Therefore, the Ce-1 alloy with high $|Z|$ at low frequencies and large phase angles in the mid-frequency region underscores its exceptional corrosion performance.

An equivalent circuit diagram, as depicted in the inset of Fig. 5(c), was employed to fit the EIS data. This circuit model is frequently utilized to elucidate the electrochemical reactions occurring at the interface between passivated metals and their substrate-solution environment[33-35]. In this model, R_s is the solution resistance, R_f is the passivated film resistance, Q_f is the passivation film capacitance, R_{ct} is the charge transfer resistance, Q_{dl} is constant phase angle elements (CPE), which represents the non-ideal capacitance behavior. Specifically, CPE can be interpreted as encompassing both the passivated film capacitance and the non-ideal double-layer capacitance. The mathematical expression for CPE is provided as follows[46]:

$$Z = \frac{1}{Q(j\omega)^n} \quad (1)$$

where Q represents the CPE's modulus value, j is the imaginary unit, ω denotes the angular frequency, and n is the CPE coefficient, ranging from 0 to 1, with n=1 signifying ideal capacitance.

The results of the equivalent circuit fitting are presented in Table 5, where the polarization resistance (R_p) is given by the following equation[47]:

$$R_p = R_s + R_f + R_{ct} \quad (2)$$

Notably, the incorporation of Ce significantly enhances the R_p values of CoCrNi MEAs, with the Ce-1 alloy exhibiting the highest R_p value, approximately double that of the Ce-0 alloy. A higher R_p value is indicative of superior corrosion resistance for the alloy[47]. Consequently, the Ce-1 alloy emerges as the most corrosion-resistant, followed by the Ce-2 alloy, while the Ce-0 alloy displays the lowest resistance. These findings are in accordance with the results obtained from the potentiodynamic polarization tests.

Figure 6 displays SEM images of CoCrNi MEAs after undergoing potentiodynamic polarization in a 3.5wt.% NaCl solution, with varying Ce contents. All Ce micro-alloyed MEAs exhibit similar corrosion mechanisms, characterized by varying degrees of pitting. A comparison of the sample before (Fig. 2) and after the potentiodynamic polarization reveals that the locations of pitting corrosion closely correspond to the positions of precipitates, suggesting that corrosion preferentially initiates in the vicinity of precipitates. Notably, the Ce-1 alloy demonstrates the lowest pit density and the best surface integrity, indicative of superior corrosion resistance. Compared to the other two alloys, the Ce-2 alloy displays severe corrosion, with

Table 5: Fitting results of EIS data for CoCrNi MEAs samples with different Ce contents

Alloys	R_s (Ω·cm^2)	R_f (Ω·cm^2)	Q_f (Ω^{-1}·cm^2·S^n)	R_{ct} (kΩ·cm^2)	Q_{dl} (Ω^{-1}·cm^2·S^n)	R_p (kΩ·cm^2)	χ^2×10^{-3}
Ce-0	10.31	18.91	2.854×10^{-5}	75.19	6.886×10^{-5}	75.219	0.2246
Ce-1	8.976	27.59	5.141×10^{-5}	157.2	3.652×10^{-5}	157.236	0.3612
Ce-2	8.814	17.06	2.026×10^{-5}	110.0	5.777×10^{-5}	110.026	0.5985

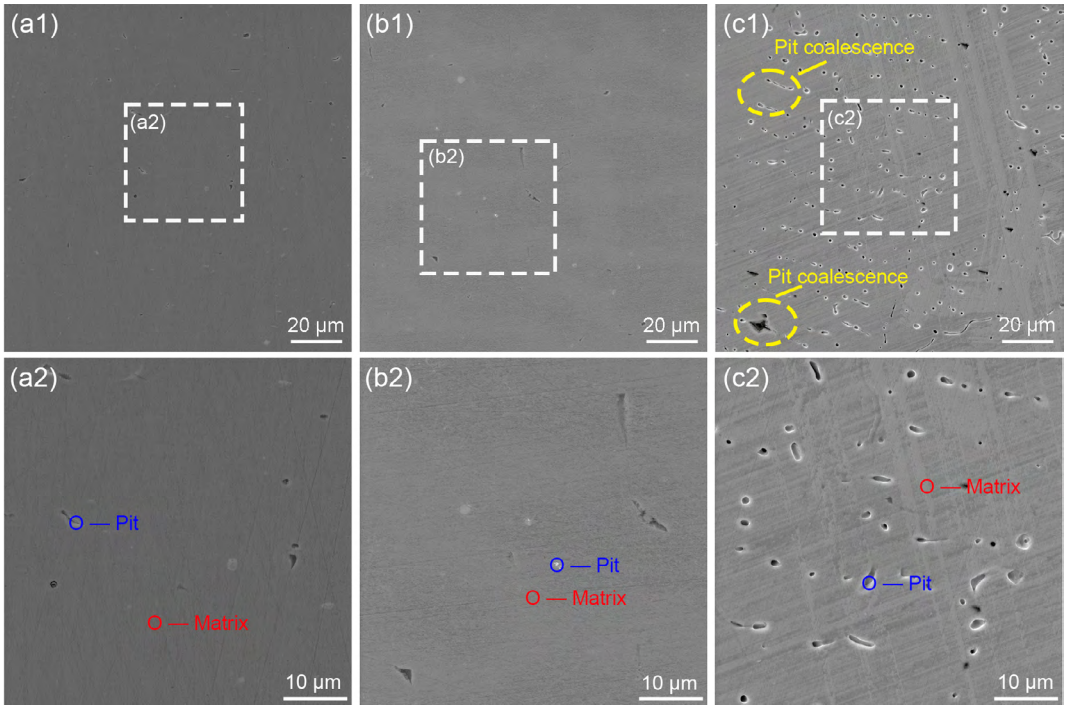

Fig. 6: SEM images of CoCrNi MEAs after potentiodynamic polarization with different Ce contents: (a) Ce-0; (b) Ce-1; (c) Ce-2

pits evolving from circular to elliptical shapes and coalescing, leading to decreased corrosion resistance.

EDS analysis presented in Table 6 reveals that at the edges of the pits, the concentrations of Co and Ni decrease, while the concentration of Cr increases. This suggests that the selective dissolution of Co and Ni is a driving force for the formation of pitting corrosion[48]. Furthermore, the presence of residual Ce within the pits of the Ce-1 alloy indicates that corrosion preferentially initiates in the vicinity of the precipitated phase.

3.3 Analysis of passivation film composition

The XPS analysis of the surface elements in the passivation films of Ce-0 and Ce-1 alloys after 7 days of immersion in a 3.5wt.% NaCl solution is depicted in Fig. 7. The surface morphology of the alloys undergoes significant changes, with the Ce-0 alloy exhibiting more severe corrosion [Fig. 7(a)]. In the XPS spectrum of the Ce-0 alloy, the Co 2p peaks correspond to metal Co^0 (776.52 eV), Co_2O_3 (781.34 eV), $Co(OH)_2$ (784.19 eV), and satellite peaks (Co_{sat}) at 787.64 eV [Fig. 7(d1)]. The Cr 2p spectrum in Fig. 7(d2) reveals peaks for Cr^0 (573.69 eV) and $Cr(OH)_3$ (577.54 eV), suggesting the presence of $Cr(OH)_3$ in the passivation film. The Ni 2p spectrum in Fig. 7(d3) displays peaks at 853.09 eV and 856.49 eV, which correspond to NiO and $Ni(OH)_2$, respectively.

For the Ce-1 alloy, the Co 2p spectrum in Fig. 7(e1) exhibits two peaks, representing metal Co^0 (777.82 eV) and oxide CoO (780.25 eV). The Cr 2p spectrum in Fig. 7(e2) displays two peaks, corresponding to Cr^0 (573.67 eV) and Cr_2O_3 (576.68 eV), confirming the presence of Cr_2O_3 in the passivation film. The Ni 2p spectrum in Fig. 7(e3) shows peaks at 852.28 eV and 855.67 eV, which correspond to Ni^0 and $Ni(OH)_2$, respectively. Notably, although the element Ce is not detected in the XPS analysis of the Ce-1 alloy, a comparison of the valence states of the elements between the Ce-1 and Ce-0 alloys reveals that the addition of Ce significantly influences the passivation process on the alloy's surface[49-51].

Table 6: EDS results of CoCrNi MEAs with different Ce contents in Fig. 6

Alloy	Regions	Elements (at.%)					
		Co	Cr	Ni	Ce	Hf	Zr
Ce-0	Matrix	35.62	11.86	52.52			
	Pit	25.25	16.44	40.18		11.85	6.27
Ce-1	Matrix	25.26	39.14	35.60			
	Pit	2.21	39.04	0.65	58.10		
Ce-2	Matrix	23.47	43.03	33.50			
	Pit	15.85	68.89	15.26			

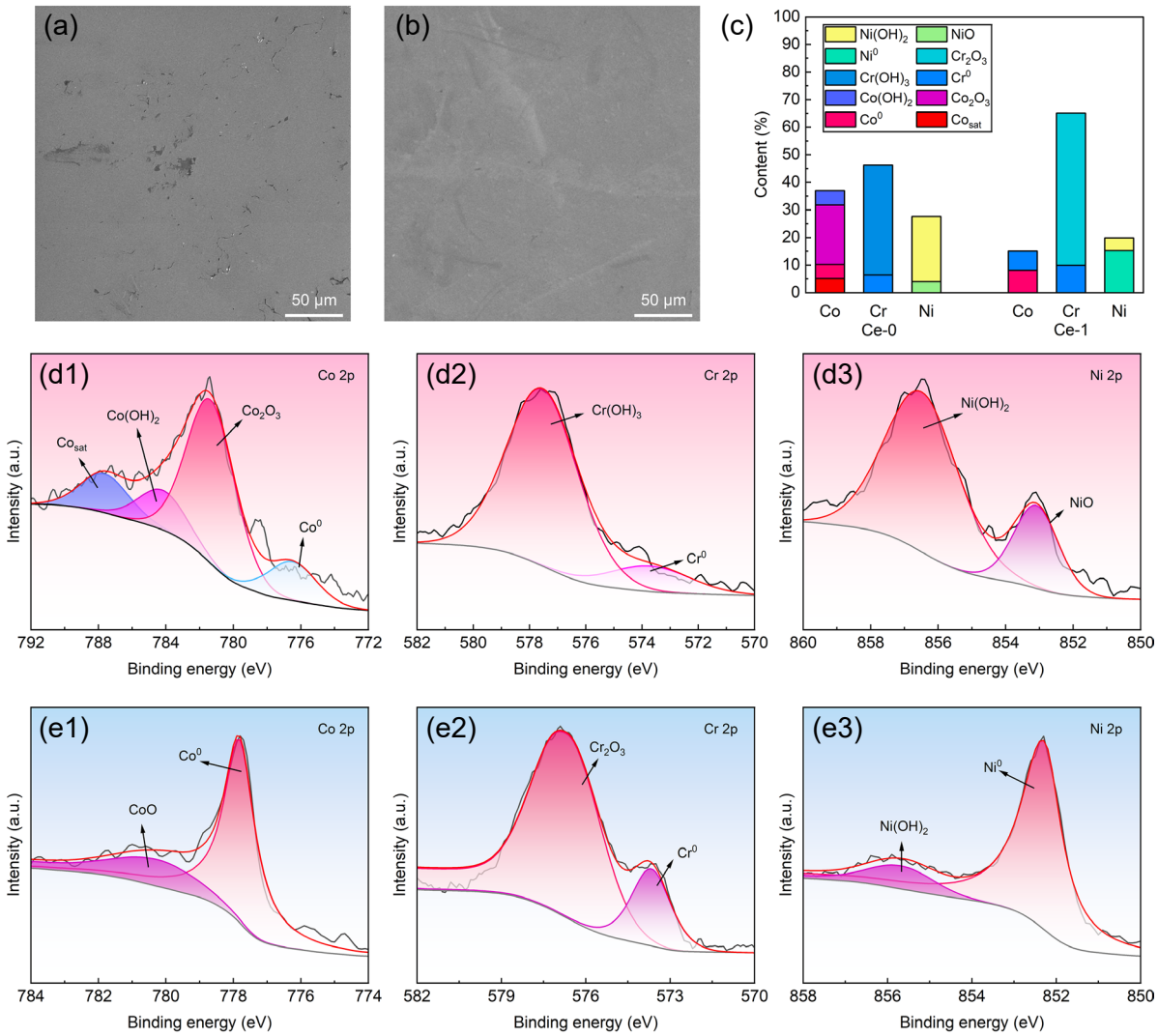

Fig. 7: Surface passivation film morphology and XPS results of Ce-0 (a, d1–d3) and Ce-1 (b, e1–e3) alloys: (a) and (b) SEM images of the alloys' surface passivation films; (c) XPS quantitative analysis; (d1) and (e1) Co; (d2) and (e2) Cr; (d3) and (e3) Ni

Figure 7(c) presents a comparison of the elemental content and valence states in the passivation films of Ce-0 and Ce-1 alloys. As evident from the Fig. 7(c), there are significant differences in the morphology and content of Co, Cr, and Ni in the passivation films of the two alloys. Specifically, the Ce-1 alloy contains notably more Cr and less Co and Ni compared to the Ce-0 alloy. Furthermore, in the Ce-0 alloy, the passivation film primarily consists of hydroxides of Ni and Cr, along with oxides of Co. Conversely, in the Ce-1 alloy, the passivation film is mainly composed of oxides of Cr. Clearly, Ce micro-alloying has a substantial impact on the passivation process and the composition of passivation films in CoCrNi MEAs[52]. The composition and structure of the passivation film are intimately linked to the corrosion resistance of the alloy, with studies indicating that Cr-rich oxide films exhibit greater stability, fewer defects, and enhanced corrosion resistance[50, 53]. Consequently, the improved corrosion resistance of CoCrNi MEAs with the addition of Ce can be attributed to the alterations in the elemental content and morphology of the passivation film.

3.4 Corrosion mechanism

The corrosion mechanism of CoCrNi MEAs with varying Ce content is depicted in Fig. 8. Specifically, for CoCrNi MEAs [Fig. 8(a)], when exposed to a 3.5wt.% NaCl solution, a passivation film comprising oxides and hydroxides forms on the alloy's surface[32, 34]. Initially, due to the presence of oxidized inclusions, these inclusions serve as the anodic phase, creating a micro-galvanic corrosion cell system with the cathodic phase of the MEAs substrate. This results in the electrochemical dissolution of the inclusions and the initiation of pitting corrosion. As corrosion progresses, harmful ions, such as chloride (Cl^-), accumulate within the pits[54-56], further exacerbating the corrosion process. Over time, the oxidized inclusions completely dissolve, leaving behind stable pitting pits.

In Ce micro-alloyed MEAs [Fig. 8(b)], the precipitated Ce phase adopts a core-shell structure, with RE-O forming the core and RE-O-S comprising the shell. Studies have demonstrated that this type of precipitate is electrically non-conductive[23, 57], undergoing chemical dissolution during

the corrosion process. Given the differential dissolution rates (RE-O-S>RE-O)[57], RE-O-S undergoes preferential chemical dissolution in NaCl solutions, leading to the formation of corrosion pits. As time progresses, ions such as sulfide (S^{2-}) and hydrogen (H^{+}), originating from the dissolution of RE-O-S, accumulate within the pits, creating localized acidic zones[57]. These acidic zones ultimately result in the complete dissolution of the RE-O component within the precipitated phase.

Based on the aforementioned analysis, the enhanced corrosion performance of as-cast CoCrNi MEAs following Ce micro-alloying can be attributed to several factors. Firstly, Ce micro-alloying alters the characteristics, such as morphology and size, and type of inclusions[51], thereby reducing the possibility to form localized electrochemical corrosion cells between the inclusions and the matrix. This attenuation of localized electrochemical corrosion subsequently enhances the corrosion resistance of the alloy. Furthermore, the incorporation of Ce increases the Cr_2O_3 content within the passivation film, further bolstering the corrosion resistance[58]. Additionally, the unique non-conductive nature of the Ce-precipitated phase[23, 57] further augments the corrosion resistance of CoCrNi MEAs by decreasing the number of active sites on the alloy surface susceptible to corrosion. Conversely, elevated Ce concentrations lead to an increased abundance of non-conducting precipitate, which undergo chemical dissolution, impairing the integrity of the surface passivation film and consequently degrading the corrosion resistance of the alloy. While this localized effect is evident in the microstructural characterization, electrochemical measurements (including potentiodynamic polarization curves and EIS) consistently reveal that the overall corrosion performance of the Ce-1 and Ce-2 alloys still surpasses that of the Ce-0 alloy.

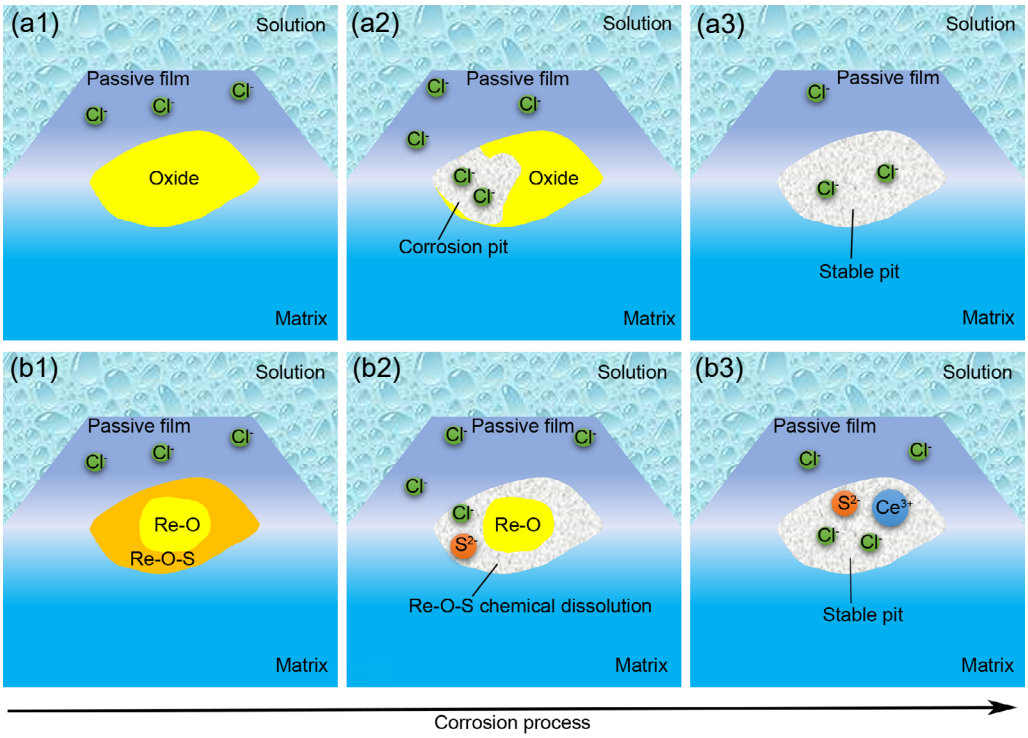

Fig. 8: Corrosion mechanism diagrams of CoCrNi MEAs (a) and Ce micro-alloyed MEAs (b)

4 Conclusions

This study examined the effects of Ce micro-alloyed on the microstructure and corrosion behavior of as-cast CoCrNi MEAs in a 3.5wt.% NaCl solution. The key findings are summarized as follows:

(1) Ce micro-alloyed MEAs maintain a single FCC structure. Ce-rich oxide precipitates appear in Ce micro-alloyed MEAs, with their amount increases with the increase of Ce content and tends to segregate to the interdendritic regions.

(2) The corrosion resistance of Ce micro-alloyed MEAs initially increases and then decreases with increasing Ce content. The optimal corrosion performance of Ce micro-alloyed MEAs is achieved at a Ce content of 0.02at.%, characterized by the widest passivation range (ΔE=0.996 V), the highest breakdown potential (E_b=0.471 V), and the lowest passivation current density (I_{pass}=26.383 μA·cm^{-2}).

(3) The improved corrosion resistance is attributed to the influence of Ce micro-alloyed on inclusions. Ce micro-alloying alters the characteristics, such as morphology and size, and type of inclusions, specifically the formation of a non-conductive Ce-rich oxide precipitate phase. Furthermore, the incorporation of Ce increases the Cr_2O_3 content within the passivation film, further bolstering the corrosion resistance.

Acknowledgments

This work was financially supported by the Natural Science Foundation of China (52264055), the Natural Science Foundation of Inner Mongolia Autonomous Region

(2024MS05038), the Open Project of State Key Laboratory of Advanced Special Steel, the Shanghai Key Laboratory of Advanced Ferrometallurgy, Shanghai University (SKLASS 2023-05), the Science and Technology Commission of Shanghai Municipality (19DZ2270200), the Fundamental Research Funds for Inner Mongolia University of Science & Technology (2024QNJS086), the Rare Earth Advanced Materials Technology Innovation Center (0904052404), and the Program for Innovative Research Team in Universities of Inner Mongolia Autonomous Region (NMGIRT2401).

Conflict of interest

The authors declare that they have no known competing financial interests or personal relationships that could have appeared to influence the work reported in this paper.

References

[1] Liu D, Yu Q, Kabra S, et al. Exceptional fracture toughness of CrCoNi-based medium- and high-entropy alloys at 20 Kelvin. Science, 2022, 378(6623): 978–983.
[2] Gludovatz B, Hohenwarter A, Thurston K V S, et al. Exceptional damage-tolerance of a medium-entropy alloy CrCoNi at cryogenic temperatures. Nat. Commun., 2016, 7: 10602.
[3] Wu Z, Bei H, Pharr G M, et al. Temperature dependence of the mechanical properties of equiatomic solid solution alloys with face-centered cubic crystal structures. Acta Mater., 2014, 81: 428–441.
[4] Guan H Q, Huang S S, Ding J H, et al. Chemical environment and magnetic moment effects on point defect formations in CoCrNi-based concentrated solid-solution alloys. Acta Mater., 2020, 187: 122–134.
[5] Cao F H, Chen Y, Zhao S T, et al. Grain boundary phase transformation in a CrCoNi complex concentrated alloy. Acta Mater., 2021, 209: 116786.
[6] Ma Y, Yuan F P, Yang M X, et al. Dynamic shear deformation of a CrCoNi medium-entropy alloy with heterogeneous grain structures. Acta Mater., 2018, 148: 407–418.
[7] Zhu M, He F, Yuan Y F, et al. A comparative study on the corrosion behavior of CoCrNi medium-entropy alloy and 316L stainless steel in simulated marine environment. Intermetallics, 2021, 139: 107370.
[8] Wang D P, Shen J W, Chen Z, et al. Relationship of corrosion behavior between single-phase equiatomic CoCrNi, CoCrNiFe, CoCrNiFeMn alloys and their constituents in NaCl solution. Acta Metall. Sin. (Engl. Lett.), 2021, 34(11): 1574–1584.
[9] Agustianingrum M P, Lee U, Park N. High-temperature oxidation behaviour of CoCrNi medium-entropy alloy. Corros. Sci., 2020, 173: 108755.
[10] Laplanche G, Kostka A, Reinhart C, et al. Reasons for the superior mechanical properties of medium-entropy CrCoNi compared to high-entropy CrMnFeCoNi. Acta Mater., 2017, 128: 292–303.
[11] Zhou Y, Zeng S, Zhang H, et al. Tailoring microstructures and mechanical properties of $Zr_{45}Ti_{15}Nb_{30}Ta_{10}$ refractory complex concentrated alloy using warm-rolling. J. Mater. Res. Technol., 2024, 187: 101–112.
[12] Chen J Q, Zhou Y K, Yu L L, et al. Enhancing strength-ductility combination of Fe-Ni-Cr-Al-Ti high-entropy alloys via co-precipitation of sigma and $L2_1$ phases. Mat. Sci. Eng. A, 2024, 913: 147062.
[13] Du C C, Jin S B, Fang Y, et al. Ultrastrong nanocrystalline steel with exceptional thermal stability and radiation tolerance. Nat. Commun., 2018, 9(1): 5389.
[14] Zhang B, Wang J, Wu B, et al. Unmasking chloride attack on the passive film of metals. Nat. Commun., 2018, 9(1): 2559.
[15] Zhang L J, Zhang M D, Zhou Z, et al. Effects of rare-earth element, Y, additions on the microstructure and mechanical properties of CoCrFeNi high entropy alloy. Mat. Sci. Eng. A–Struct., 2018, 725: 437–446.
[16] Jiang H, Jiang L, Qiao D, et al. Effect of niobium on microstructure and properties of the $CoCrFeNb_xNi$ high entropy alloys. J. Mater. Sci. Technol., 2017, 33(7): 712–717.
[17] Zhang Y Y, Wu H B, Yu X P, et al. Microstructural evolution and strengthening mechanisms in $Cr_xMnFeNi$ high-entropy alloy. J. Mater. Res. Technol., 2021, 12: 2114–2127.
[18] Wang Y, Li G L, Qi H, et al. Effect of Al content on the corrosion behavior and mechanism of $Al_xCoCrFeNi$ high-entropy alloys. J. Mater. Res. Technol., 2024, 30: 5977–5989.
[19] Zhang T, Xin L J, Wu F F, et al. Microstructure and mechanical properties of $Fe_xCoCrNiMn$ high-entropy alloys. J. Mater. Sci. Technol., 2019, 35(10): 2331–2335.
[20] Singh H, Xiong Y, Rani E, et al. Unveiling nano-scaled chemical inhomogeneity impacts on corrosion of Ce-modified 2507 super-duplex stainless steels. NPJ Mater. Degrad., 2022, 6(1): 1–10.
[21] Zhang L M, Zhang S D, Ma A L, et al. Influence of cerium content on the corrosion behavior of Al-Co-Ce amorphous alloys in 0.6 M NaCl solution. J. Mater. Sci. Technol., 2019, 35: 1378–1387.
[22] Wang C G, Ma R Y, Zhou Y T, et al. Effects of rare earth modifying inclusions on the pitting corrosion of 13Cr4Ni martensitic stainless steel. J. Mater. Sci. Technol., 2021, 93: 232–243.
[23] Lu P C, Zhang P F, Feng H, et al. Revealing the impact of inclusion types on pitting corrosion behavior of high-nitrogen stainless bearing steels with different Ce contents: Induction effect of oxides/sulfides and inhibition effect of nitrides. Corros. Sci., 2024, 236: 112247.
[24] Li M X, Wang C, Li Y J, et al. Tailoring the microstructure and enhancing the corrosion resistance of extruded dilute Mg-0.6Al-0.5Mn-0.25Ca alloy by adding trace Ce. Corros. Sci., 2022, 207: 110605.
[25] Jin Z Z, Zha M, Wang D W, et al. Influence of Ce micro-alloying on the microstructure and corrosion behavior of sub-rapid solidified Mg-4.5Al-1.5Sn-0.5Ca alloys. J. Mater. Res. Technol., 2023, 26: 3768–3783.
[26] Lin Y S, Lu Y C, Hsueh C H. Strengthening of CoCrNi medium entropy alloy with gadolinium additions. Vacuum, 2023, 211: 111969.
[27] Chan S N, Hsueh C H. Effects of La addition on the microstructure and mechanical properties of CoCrNi medium entropy alloy. J. Alloys Compd., 2022, 894: 162401.
[28] Xing L, Wang H Y, Gao X Y, et al. Effects of Ce addition on inclusion modification in martensitic stainless steel. Mater. Res. Express, 2024, 11(7): 76515.
[29] Yu Y H, Feng X M, Luo D Q, et al. Effect of rare earth Ce addition on inclusions in offshore engineering steel containing arsenic. Mater. Res. Express, 2023, 10(11): 116512.
[30] Yin B S, Hu X J, Lu Z P, et al. The effect of Ce addition on purification and inclusion modification of cocrfenimn high entropy alloy. J. Alloys Compd., 2023, 934: 167716.
[31] Duan J F, Lan A D, Jin X, et al. Irregular pitting propagation within the inclusions in Ce-doped $Fe_{40}Mn_{20}Cr_{20}Ni_{20}$ high-entropy alloy. J. Alloys Compd., 2023, 968: 171881.

[32] Tian W M, Du N, Li S M, et al. Metastable pitting corrosion of 304 stainless steel in 3.5% NaCl solution. Corros. Sci., 2014, 85: 372–379.
[33] Zhang Z J, Yuan T C, Li R D. Corrosion performance of selective laser-melted equimolar CrCoNi medium-entropy alloy vs its cast counterpart in 3.5 wt% NaCl. J. Alloys Compd., 2021, 864: 158105.
[34] Zhang C L, Zhu M, Yuan Y F, et al. Comparison of corrosion behavior of CoCrNi medium-entropy alloy with CoCrFeMnNi high-entropy alloy in SO_2-polluted marine environment. J. Mater. Eng. Perform., 2024, 33(2): 541–555.
[35] Luo H, Zou S, Chen Y, et al. Influence of carbon on the corrosion behaviour of interstitial equiatomic CoCrFeMnNi high-entropy alloys in a chlorinated concrete solution. Corros. Sci., 2020, 163: 108287.
[36] Li M W, Nutor R K, Cao Q P, et al. Corrosion behavior of Al-containing CoNiV alloys. Corros. Sci., 2022, 207: 110567.
[37] Han Z H, Guo C H, Huang C D, et al. Corrosion resistant body-centered cubic VNbTa refractory medium-entropy alloy. Corros. Sci., 2024, 229: 111885.
[38] Chen J L, Feng Z X, Yi J H, et al. Effect of low temperature rolling on mechanical properties and corrosion resistance of CrCoNi medium entropy alloy. Mater. Res. Express., 2022, 9(1): 16502.
[39] Wei R, Jiang Z, Gao Q Y, et al. A comparison of the mechanical and corrosion behavior of $Fe_{49.5}Mn_{25}Cr_{15}Ni_{10}C_{0.5}$ medium-entropy alloy with its subsystems steels. Intermetallics, 2022, 151: 107736.
[40] Zhao R F, Ren B, Cai B, et al. Corrosion behavior of Co_xCrCuFeMnNi high-entropy alloys prepared by hot pressing sintered in 3.5% NaCl solution. Results Phys., 2019, 15: 102667.
[41] Qiu X W, Liu C G. Microstructure and properties of Al_2CrFeCoCuTiNi high-entropy alloys prepared by laser cladding. J. Alloys Compd., 2013, 553: 216–220.
[42] Öztürk S, Alptekin F, Önal S, et al. Effect of titanium addition on the corrosion behavior of CoCuFeNiMn high entropy alloy. J. Alloys Compd., 2022, 903: 163867.
[43] Shi Z J, Wang Z B, Wang X D, et al. Effect of thermally induced B2 phase on the corrosion behavior of an $Al_{0.3}$CoCrFeNi high entropy alloy. J. Alloys Compd., 2022, 903: 163886.
[44] Gu D D, Zhang H, Dai D H, et al. Anisotropic corrosion behavior of Sc and Zr modified Al-Mg alloy produced by selective laser melting. Corros. Sci., 2020, 170: 108657.
[45] Luo H, Li Z, Mingers A M, et al. Corrosion behavior of an equiatomic CoCrFeMnNi high-entropy alloy compared with 304 stainless steel in sulfuric acid solution. Corros. Sci., 2018, 134: 131–139.
[46] Hirschorn B, Orazem M E, Tribollet B, et al. Determination of effective capacitance and film thickness from constant-phase-element parameters. Electrochim. Acta, 2010, 55(21): 6218–6227.
[47] Wang J Y, Li W H, Yang H L, et al. Corrosion behavior of CoCrNi medium-entropy alloy compared with 304 stainless steel in H_2SO_4 and NaOH solutions. Corros. Sci., 2020, 177: 108973.
[48] Zhu M, Zhang C L, Yuan Y F, et al. The corrosion behavior of CoCrNi medium entropy alloy with alternating current interference in carbonate/bicarbonate solution. J. Mater. Eng. Perform., 2023, 32(1): 1–17.
[49] Song L F, Hu W B, Huang S Y, et al. Electrochemical behavior and passive film properties of Ce-added $AlCoCrFeNi_{2.1}$ eutectic high-entropy alloys in sulfuric acid solution. J. Electroanal. Chem., 2023, 950: 117883.
[50] Feng H, Li H B, Wu X L, et al. Effect of nitrogen on corrosion behaviour of a novel high nitrogen medium-entropy alloy CrCoNiN manufactured by pressurized metallurgy. J. Mater. Sci. Technol., 2018, 34(10): 1781–1790.
[51] Ha H, Park C, Kwon H. Effects of misch metal on the formation of non-metallic inclusions and the associated resistance to pitting corrosion in 25% Cr duplex stainless steels. Scr. Mater., 2006, 55(11): 991–994.
[52] Guo Q, Liu B, Li Q, et al. Effect of 0.3 at.% Ce on the corrosion resistance of $Fe_{40}Ni_{20}Co_{20}Cr_{20}$ high-entropy alloy in 3.5 wt% NaCl solution. Mater. Lett., 2024, 364: 136310.
[53] Luo H, Su H Z, Dong C F, et al. Passivation and electrochemical behavior of 316L stainless steel in chlorinated simulated concrete pore solution. Appl. Surf. Sci., 2017, 400: 38–48.
[54] He F, Zhu M, Yuan Y F, et al. Synergistic effect of HCO_3^- and alternating current on corrosion behavior of CoCrNi medium-entropy alloy in simulated marine environment. J. Mater. Eng. Perform., 2024, 33(16): 8372–8385.
[55] He F, Zhu M, Yuan Y F, et al. Study on AC corrosion behavior of CoCrNi medium-entropy alloy in 3.5% NaCl solution. J. Mater. Eng. Perform., 2023, 32(7): 2918–2931.
[56] Zhang Y H, Hu Q, Dai M J, et al. Investigation of micro-electrochemical activities of oxide inclusions and microphases in duplex stainless steel and the implication on pitting corrosion. Mate. Corros., 2020, 71(6): 876–886.
[57] Liu X J, Yang C Q, Ren H P, et al. Origin mechanism of pitting corrosion induced by cerium inclusions. J. Rare Earths., 2023, 41(9): 1448–1458.
[58] Cheng Z Z, Dong L A, Min Z, et al. Effect of Ce on the localized corrosion behavior of non-equiatomic high-entropy alloy $Fe_{40}Mn_{20}Cr_{20}Ni_{20}$ in 0.5 M H_2SO_4 solution. Corros. Sci., 2022, 206: 110489.